Transport in Asymmetrically Coupled Donor-Based Silicon Triple Quantum Dots

6 **AUTHORS**, INCLUDING:

Thomas F Watson

10 PUBLICATIONS   50 CITATIONS

SEE PROFILE

Bent Weber

Monash University (Australia)

21 PUBLICATIONS   284 CITATIONS

SEE PROFILE

Jill A. Miwa

Aarhus University

52 PUBLICATIONS   747 CITATIONS

SEE PROFILE

Michelle Simmons

University of New South Wales

436 PUBLICATIONS   7,136 CITATIONS

SEE PROFILE

Transport in Asymmetrically Coupled Donor-Based Silicon Triple Quantum Dots

Thomas F. Watson,[†] Bent Weber,[†] Jill A. Miwa,[†,‡] Suddhasatta Mahapatra,[†,¶] Roel M. P. Heijnen,[†] and Michelle Y. Simmons*,[†]

[†]Australian Research Council Centre of Excellence for Quantum Computation and Communication Technology, University of New South Wales, Sydney, New South Wales 2052, Australia

S *Supporting Information*

ABSTRACT: We demonstrate serial electron transport through a donor-based triple quantum dot in silicon fabricated with nanoscale precision by scanning tunnelling microscopy lithography. From an equivalent circuit model, we calculate the electrochemical potentials of the dots allowing us to identify ground and excited states in finite bias transport. Significantly, we show that using a scanning tunnelling microscope, we can directly demonstrate that a ~1 nm difference in interdot distance dramatically affects transport pathways between the three dots.
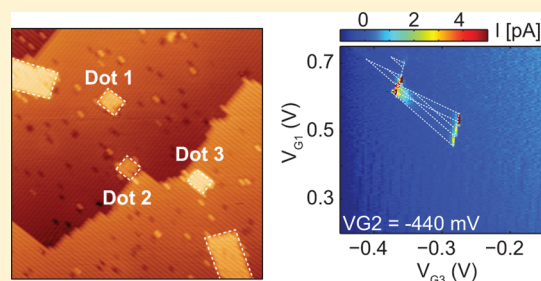
KEYWORDS: STM lithography, triple quantum dots, silicon, finite bias spectroscopy, Si:P

Qubits based on electron spins confined to quantum dots or shallow donors in silicon are promising candidates for scalable quantum computing with extremely long coherence times reaching up to seconds in isotropically purified ^{28}Si.[1,2] Proposals for a scalable architecture require arrays of donor qubits separated by a few tens of nanometers and placed with atomic precision.[3,4] Nonlocal coupling between qubits is important for reducing the fault-tolerant error threshold and can be achieved by incorporating a coherent transport method into the architecture.[4,5] A number of methods that use linear arrays of donors to transport electron spin qubits have been proposed such as spin shuttling,[6] spin buses,[7,8] and coherent transport by adiabatic passage (CTAP).[9]

Three serially coupled donor dots represent the smallest possible system in which these transport methods can be investigated and, consequently, are a fundamental building block for scalable architectures. Beyond spin transport, they also form the basis of an "exchange only" qubit in which only exchange coupling between the electrons in adjacent dots is needed to perform one and two qubit operations allowing for all electrical control.[10−13] With the potential for exchange pulses on subnanosecond time scales[14] and coherence times 2 orders of magnitude greater than those measured in GaAs QDs,[15] triple donor systems are promising candidates for scalable quantum computing in silicon.

To realize both spin transport and the "exchange only" qubit, it is necessary to have full electrostatic control of the donor dots and to tailor the interdot tunnel coupling, which is challenging to achieve at small interdot separations.[16,17] Consequently, charge stability and transport have only been investigated in GaAs[18−20] and silicon[21] triple quantum dots, several tens of nanometres in diameter and separation. Finite bias spectroscopy in coupled QD systems allows direct access to the valley-orbit spectrum and the spin degree of freedom in DC transport. Such measurements have recently been performed on the molecular states of a parallel triple quantum dot[22] and on serially coupled triple quantum dots in GaAs where spin blockade was demonstrated.[19,23] To date, however, there has been no description of finite bias transport in the full 3D stability diagram for serially coupled triple quantum dots.

Scanning tunnelling microscopy (STM)-lithography has successfully demonstrated the deterministic placement of single phosphorus donors[24] and donor-based quantum dots[17,25−28] with atomic precision inside a two-dimensional device architecture, where both DC transport and single shot spin read-out have been performed. Recently, we have achieved independent electrostatic control of two precisely positioned coupled phosphorus donor dots[17] aligned to in-plane gates in which predictive modeling with FASTCAP was used to optimize device design. In this paper, we extend this work by demonstrating independent electrostatic control of a donor-based silicon triple quantum dot (TQD) transport device, where the addition of a third dot with associated gates imposes significantly tighter constraints on this atomic-scale device architecture. With precision control over the gate alignment and the position of the dots, we gain full control over the electrochemical potentials of the three dots allowing us to resolve all six distinct quadruple points (QP) characteristic for sequential tunnelling through TQDs. Using an equivalent circuit model, we calculate the regions in the 3D stability

diagram where we expect transport to occur at finite bias and show good quantitative agreement with measured data, allowing us to extract the visible valley-orbit excited state energies.

Figure 1a shows the overall device architecture after STM lithography on a hydrogen passivated Si(001) 2 × 1
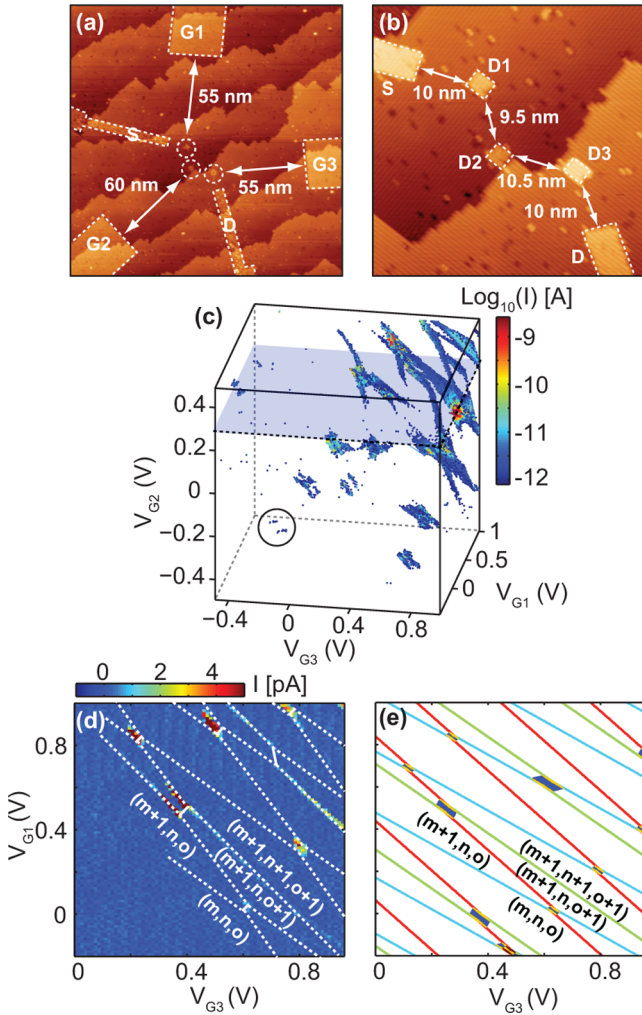

Figure 1. Donor-based serially coupled triple quantum dot. (a) Overview STM-image of the triple dot device after lithography showing the three dots (D1, D2, and D3), ~4 × 4 nm² in size, tunnel-coupled to source (S) and drain (D) electrodes and capacitively coupled to three gates (G1, G2, and G3). (b) The three dots are in a triangular configuration to maximize the capacitive control of the dots. (c) Overview of the 3D transport stability diagram measured at a SD bias of 2 mV showing the SD current as a function of the three gates. In the circled region, we perform finite bias spectroscopy. (d) A cut was taken at $V_{G2} = +300$ mV (blue plane) with the charge stability extrapolated from the visible cotunnelling current at the triple points and charge addition lines. The relative slope and separation of the charge addition lines and the number of charge stable regions is in good agreement with the modeled charge stability diagram (e).

reconstructed surface. In the lighter regions bounded by dashed lines, hydrogen has been desorbed from the surface by scanning the tip under lithographic conditions (3−5 V, 1−3 nA).[25] The hydrogen acts as a lithographic mask and the desorbed regions are selectively doped by exposing the surface to PH₃ with annealing at 350 °C. This results in an atomically abrupt planar doping profile with a one-fourth monolayer

density ($N_{2D} \approx 2 \times 10^{18}$ m⁻²).[29] In three dimensions, this equates to a doping density of $\approx 10^{21}$ cm⁻³, 3 orders of magnitude above the Mott metal−insulator transition, allowing quasimetallic conduction in all device electrodes.[30] The device is then overgrown with ≈30 nm of epitaxial Si and contacted ex situ by the deposition of aluminum ohmic contacts.[25]

A close up of the central region of the device in Figure 1b shows the three dots (D1, D2, and D3) with a lithographic size of approximately (4 × 4) nm², hosting ≈15 donors each. The adjacent dots, D1 and D2 and D2 and D3, are mutually tunnel-coupled with tunnel gaps of ≈9.5 nm and ≈10.5 nm, respectively. D1 and D3 are further tunnel-coupled to source (S) and drain (D) leads respectively, each with tunnel gaps of ≈10 nm. Direct tunnelling from S−D2, D1−D3, and D2−D is suppressed due to the large (≈ 20 nm) gaps between them, ensuring that transport occurs in series through each of the three dots. The precise position, distance, and width of all plunger gates (G1, G2, and G3) is a result of careful optimization with the finite element capacitance solver FASTCAP,[31] allowing us to control the electron occupation on each dot independently and to explore the full 3D stability diagram. This is achieved despite the small interdot distances by placing the dots in a triangular configuration, which significantly improves the ratio between the direct and cross capacitances of the gates with their respective dots.[17]

Full electrostatic control over the 3D gate space is demonstrated in Figure 1c, where we show the transport stability diagram recorded at $V_{SD} = +2$ mV at the base temperature of the dilution fridge (electron temperature ~200 mK). We plot the SD current as a function of the three gate voltages, V_{G1}, V_{G2}, and V_{G3}, and observe a number of regions of finite current, which correspond to sequential transport for different electron occupancies on the dots. To gain a detailed understanding of charge stability in atomic-scale TQDs, we model this data by determining the charge configuration on the three dots that minimizes the electrostatic energy, U, as a function of the gate voltages, V_{G1}, V_{G2}, and V_{G3}.[32,33] The electrostatic energy was calculated using an equivalent circuit model where we consider a total of 15 capacitances including all the cross capacitances between the gates and the dots (see Supporting Information),

$$U(N_1, N_2, N_3) = \sum_{i,j=1}^{3} \frac{1}{2} N_i N_j E_{i,j} + f(N_1, N_2, N_3, \vec{V}, C_{gidj})$$

(1)

Here, N_i is the number of electrons on dot i, $E_{i,j}|_{i=j}$ is its intradot charging energy, $E_{i,j}|_{i\neq j}$ is the interdot charging energy between dots i and j, f is the electrostatic energy due to charge induced by gate voltages, $\vec{V} = (V_{G1}, V_{G2}, V_{G3})$, and C_{gidj} are the capacitances of the gates to the dots. The electrochemical potentials, μ_i, of dots i, are defined as

$$\mu_1(N_1, N_2, N_3) = U(N_1, N_2, N_3) - U(N_1 - 1, N_2, N_3)$$

$$\mu_2(N_1, N_2, N_3) = U(N_1, N_2, N_3) - U(N_1, N_2 - 1, N_3)$$

$$\mu_3(N_1, N_2, N_3) = U(N_1, N_2, N_3) - U(N_1, N_2, N_3 - 1)$$

(2)

A comparison of the measured and modeled stability diagrams is shown in Figure 1d and e, respectively, where we consider a 2D slice through the 3D data in Figure 1c at $V_{G2} = +300$ mV (shaded blue plane). In the regions bounded by the

lines, the dots have fixed electronic charge, (m, n, o), where m, n, and o are the electron numbers on D1, D2, and D3 respectively. Charge transitions on the individual dots are highlighted by light blue, green, and red addition lines in the modeled data (Figure 1e), indicating charge additions to D1, D2, and D3, respectively. The dark blue regions in Figure 1e indicate where a charge reconfiguration occurs between two dots. At the intersection of two addition lines and the charge reconfiguration line, the electrochemical potential of two dots align with the source and drain leads, corresponding to a *triple point*; at this point, three charge states are degenerate. We find good quantitative agreement of the measured data with the calculated stability diagram on the basis of capacitances extracted from FASTCAP. In particular, we note that the relative slopes of the charge addition lines in the modeled data (light blue, green, and red lines in Figure 1e) and their separations match well with the dotted white lines extrapolated from the experimental data (Figure 1d). In addition, the overall number of charge stable regions for a given voltage range match well considering that at lower voltages (V_{G1}, $V_{G3} < 0.4$ V), it is difficult to resolve any current due to the larger tunnel barriers.

In serially coupled TQDs, current is expected only at *quadruple points* (QPs) in the 3D stability diagram, where four charge states are degenerate.[18] These are seen in Figure 1c as regions of finite current in blue. Each of these regions corresponds to an electron addition to each of the three dots and contain six distinct QPs, each with a different charge transport sequence.[34] Within the gating range, we observe 12 sets of QPs ultimately determined by the lever arm of the gates to the dots and the charging energy of the dots. In Figure 1c, additional current is observed outside of the quadruple points at both the triple points and along the charge addition lines due to higher order tunnelling processes. This predominantly occurs at large positive gate voltages where the tunnel barriers between the dots and the leads are reduced.

In Figure 2a, we demonstrate sequential transport through the donor dots by showing high-resolution data of the six QPs at $V_{SD} = +0.5$ mV for the charge transition highlighted by a circle in Figure 1c. At this region in gate-space, the dots are weakly coupled and the point at which each QP appears as a function of V_{G2} is determined by the relevant electrochemical potential of D2 for each QP entering the bias window.[33] The charge states and energy level diagrams for each QP with effective electron numbers are shown in Figure 2b. The latter are determined from the sequence of electron transport[33] defined by the four degenerate charge states of each QP. QP1 (QP6) is analogous to the triple points in double quantum dots where an electron (hole) sequentially tunnels through each of the dots. The other QPs involve the tunnelling of more than one particle (electron or hole) with the net effect of one electron moving from one lead to the other.

Finite bias spectroscopy in silicon QD systems allows us to obtain information on the valley-orbit spectrum. In double quantum dots, it has been shown that access to many-body excited states can be gained without the complication of being obscured by the density of states in the leads.[16,17] To date, no studies exist on the quantitative analysis of finite bias spectroscopy within the full 3D parameter space for TQDs. To bridge this gap, we model finite-bias transport and compare it to that recorded in these atomic scale TQDs, which allows us to extract estimates of the valley orbit excited state energies. Four boundary conditions define where sequential transport can occur in the 3D stability diagram,
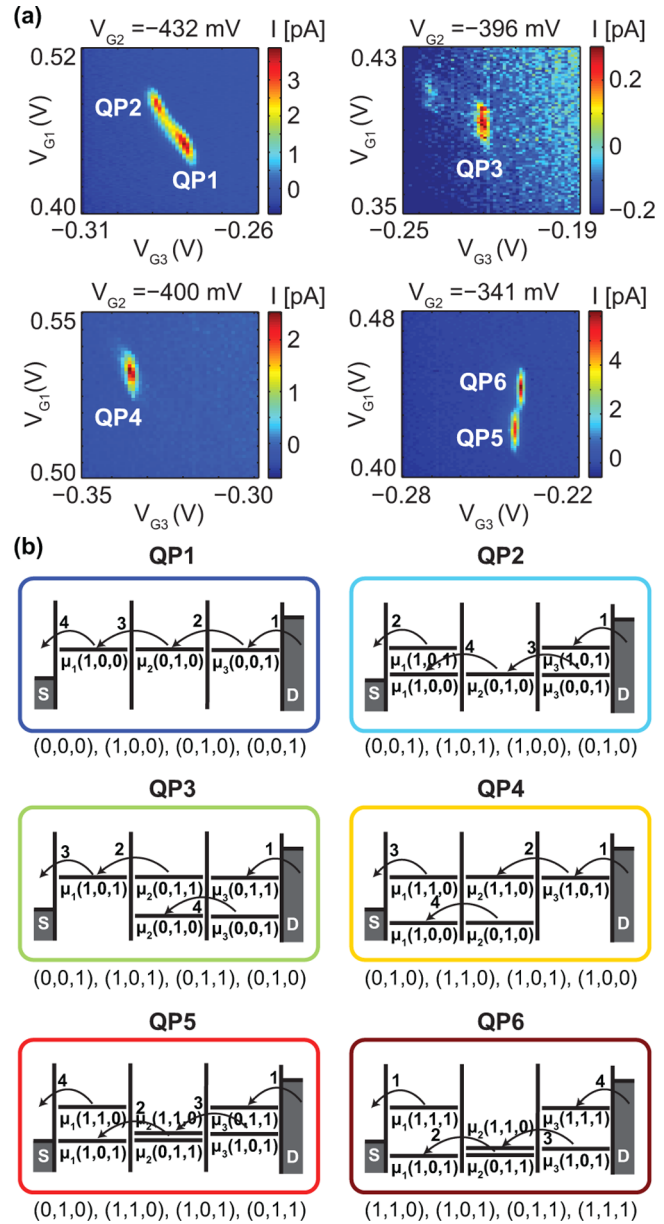

Figure 2. The six distinct quadruple points in serially coupled triple quantum dots. (a) The observation of six distinct quadruple points at the circled transition in Figure 1c measured at a SD bias of +0.5 mV. (b) The energy level diagrams for the six distinct QPs with the four degenerate charge states listed below. We use effective electron numbers and the energy level diagrams are shown for the case where the drain is grounded and a positive bias is applied to the source. The numbered arrows indicate the direction and sequence of electron transport.

$$-eV_{SD} = \mu_S \leq \mu_1 \tag{3}$$

$$\mu_1 \leq \mu_2 \tag{4}$$

$$\mu_2 \leq \mu_3 \tag{5}$$

$$\mu_3 \leq \mu_D = 0 \tag{6}$$

where μ_S and μ_D are the electrochemical potential of the source and drain lead, respectively.

Figure 3 shows the evolution of QP1 at finite bias where we show the modeled regions of transport for QP1 in the V_{G1} and
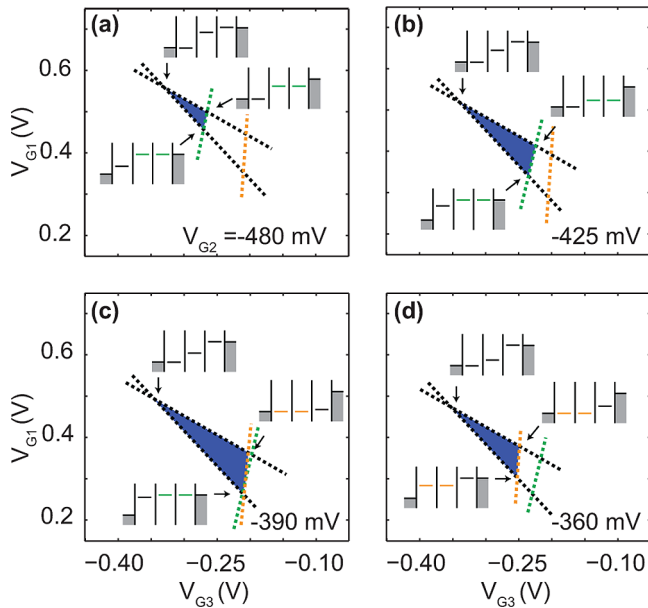
Figure 3. Evolution of quadruple point QP1 at finite bias with middle gate V_{G2}. Four boundary conditions need to be satisfied for transport to occur within a bias triangle. Two of the sides (black) are determined by the boundary conditions between D1, D3, and the leads. The base is determined by the resonance conditions between D1 and D2 (orange) and D2 and D3 (green). The V_{G2} dependence is discussed in the main text.

Figure 4. Evolution of the six quadruple points QP1−6 in the finite-bias regime. (a,b) Modeled regions of finite bias transport for two values of V_{G2} (−445 and −295 mV, respectively) at a SD bias of +10 mV. The different colored regions corresponds to the six distinct QPs as shown. The black lines at the base of the triangles correspond to the alignment of D1 and D2 (labeled 1 and 2) and D2 and D3 (labeled 3 and 4). (c,d) Measured high bias transport of the six QPs for similar values of V_{G2} (−440 and −300 mV, respectively) and at a SD bias of +10 mV. The plot shows the current as a function of V_{G1} and V_{G3}. The white lines at the base of the triangles correspond to D1 and D2 and D2 and D3 on resonance. Because of the asymmetry in the dot geometries, resonances between D1 and D2 are not observed in transport. The two additional resonances are due to cotunnelling (e) and resonant transport through an excited state (f).

V_{G3} plane at a SD bias of +10 mV and at varying V_{G2}. At high bias, each QP widens into a bias triangle in the 2D stability diagram. In the model, we treat the dots as metallic with a homogeneous density of states, and therefore, finite current is expected throughout the bias triangle. The sides of the bias triangle are determined by the boundary conditions between the leads and the dots, $-eV_{SD} \leq \mu_1$ and $\mu_3 \leq 0$ (black lines). The base of the triangle is determined by the boundary conditions $\mu_1 \leq \mu_2$ (orange line) and $\mu_2 \leq \mu_3$ (green line) when either the ground state of D1 and D2 or of D2 and D3 are in resonance. At $V_{G2} \leq -500$ mV, μ_2 is always above μ_3 within the bias window, not allowing current. As V_{G2} increases, μ_2 moves below μ_3 within the bias window and a bias triangle appears in the 2D stability diagram (Figure 3a). The base of the triangle is determined by the ground state resonance condition between D2 and D3, $\mu_2 = \mu_3$, and is shown by the green dotted line. The ground state resonance condition between D1 and D2, $\mu_1 = \mu_2$, is shown by the orange dotted line and is located at more positive V_{G3} outside the bias triangle. Here, transport is prohibited due to Coulomb blockade. As V_{G2} increases, the green dotted line moves toward more positive V_{G3} and the orange dotted line moves toward more negative V_{G3}. This increases the triangle size (Figure 3b) until there is a crossover where the base of the triangle is defined by both resonance conditions (Figure 3c). At the point where the green and orange lines intersect, all three dots are in resonance. As V_{G2} further increases, the base of the triangle is now determined by $\mu_1 = \mu_2$ (orange line) (Figure 3d). For larger V_{G2}, the triangle decreases in size until it disappears.

Figure 4 shows the modeled bias triangles for all six distinct QPs at two different values of V_{G2}, at which we would expect either D2 and D3 (Figure 4a) or D1 and D2 (Figure 4b) to be on resonance. The different colors indicated in the figure correspond to the bias triangles of the six QPs involved in
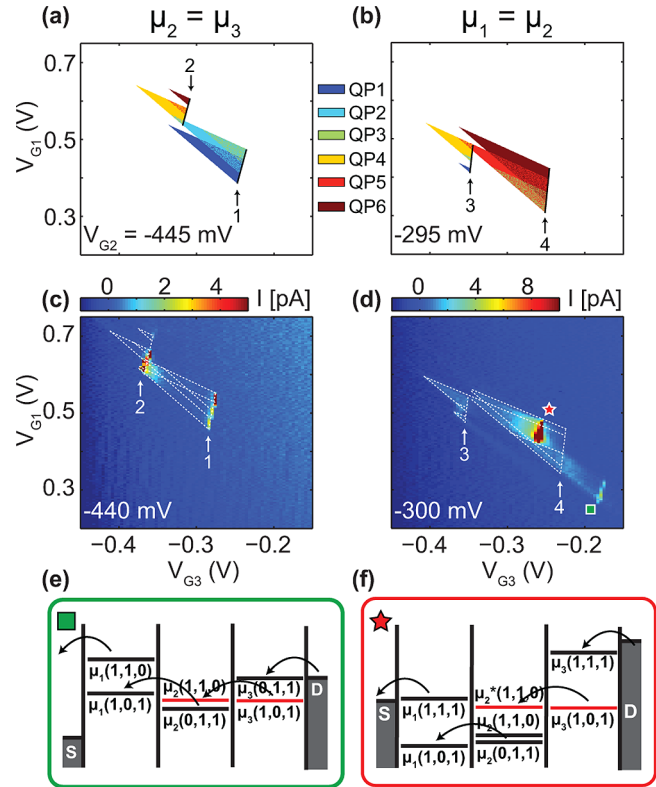
transport. In Figure 4a at $V_{G2} = -445$ mV, we find two base lines of the bias triangles corresponding to the condition $\mu_2 = \mu_3$. The first resonance (labeled 1) is between the (m, $n + 1$, o) and (m, n, $o + 1$) charge states and defines the base of the bias triangles for QP1−3 as given by the green dotted line in Figure 3a. The second resonance (labeled 2) is between the ($m + 1$, $n + 1$, o) and ($m + 1$, n, $o + 1$) charge states and differs from the first by having an additional electron on D1. At lower negative bias in Figure 4b, the two base lines now correspond to a resonance between D1 and D2 ($\mu_1 = \mu_2$). The ($m + 1$, n, o) and (m, $n + 1$, o) charge states define the base of the bias triangle (labeled 3) for QP1−2 and QP4, given by the orange dotted lines in Figure 3d. When there is an additional electron on D1 the ($m + 1$, n, $o + 1$) and (m, $n + 1$, $o + 1$) charge states define the base of the bias triangle (labeled 4) for QP3 and QP5−6.

The corresponding measured transport data is shown in Figure 4c,d recorded at $V_{SD} = +10$ mV. These are the bias triangles of the QP's shown in Figure 2a (circle Figure 1c). We note that the exact value of V_{G2} at which we present the experimental data differs slightly from the value of V_{G2} used in the simulation due to uncertainties in the capacitance extraction

from the experimental data. The evolution of the bias triangles as a function of V_{G2} is however presented in the Supporting Information Figure S2 where we observe excellent agreement. As such, we choose the V_{G2} values for the simulated data that give the best quantitative match to the experimental data. In contrast to the model, here, we observe resonances within the bias triangles due to the alignment of distinct ground and excited states in the adjacent dots. For these resonances to be observable, cotunnelling is required via the third dot. Finite off-resonance current is also observed within the triangles and results from higher order tunnelling processes.

The two ground state resonance lines between D2 and D3 are clearly seen as lines of increased current at the base of the bias triangles (Figure 4c). However, the two ground state resonance lines between D1 and D2 are not observed (Figure 4d). We can explain this by the strong asymmetry predicted in the tunnel coupling between the respective dots, with D2 and D3 being more weakly coupled than D1 and D2. The origin of this asymmetry becomes clear when we consider the STM image of the central part of the device in Figure 1b, where the distance between D1 and D2 is smaller by ∼1 nm compared to the distance between D2 and D3. This small asymmetry is reflected by a significantly larger mutual capacitance between D1 and D2 (0.5 aF) compared to D2 and D3 (0.35 aF), extracted from the high bias data. As a consequence, D1−D2 resonances are not observed because the weak tunnel coupling between D2 and D3 does not allow current to flow when D3 is off resonance. However, the strong tunnel coupling between D1 an D2 permits D2−D3 resonances to be observed via cotunnelling through D1. This demonstrates the critical role of nanometer-scale precision donor placement to control tunnel coupling in these multiquantum dot devices.

In addition to the absence of resonance current when D1 and D2 are on resonance at $V_{G2} = -300$ mV, two additional resonance lines are observed that are not seen in the model. The first (marked by the green square) is the same resonance labeled 2 in Figure 4c at $V_{G2} = -440$ mV between D2 and D3 involving the $(m + 1, n + 1, o)$ and $(m + 1, n, o + 1)$ charge states. Here, the electrochemical potential of D1 is above that of D2 and D3 (Figure 4e), so the system is in Coulomb blockade. However, it is likely that the finite current observed arises from cotunnelling via D1 to the source, consistent with D1 and D2 being more strongly coupled. The second resonance line marked by the red star is the first visible excited state resonance between D2 and D3 involving the $(m + 1, n + 1, o)$ and $(m + 1, n, o + 1)$ charge states (Figure 4f). From the gate voltage difference between the ground and excited states and with a gate lever arm $\alpha = 0.10e$ (see Supporting Information), we find $\Delta E = 3.4$ meV, comparable in magnitude with excited state energies recently observed in donor-based double quantum dots of similar size.[17]

In conclusion, we have demonstrated finite bias spectroscopy in a serially coupled donor-based triple quantum dot device. Combining the ability to access the full 3D parameter space of TQDs with an equivalent circuit model, we are able to identify discrete ground and excited state resonances in transport and demonstrate that using an STM to directly measure the dot locations we can understand the strong asymmetric coupling of the quantum dots. Both the subnanometer precision placement of donors and the full electrostatic control of the dot potentials will be critical for the control over exchange coupling toward the realization of spin transport protocols and the "exchange only" qubit.

■ ASSOCIATED CONTENT

Ⓢ Supporting Information

The equivalent circuit model and extraction of the first visible excited state energy. This material is available free of charge via the Internet at http://pubs.acs.org/.

■ AUTHOR INFORMATION

Corresponding Author

*M. Y. Simmons. E-mail: michelle.simmons@unsw.edu.au.

Present Addresses

‡Department of Physics and Astronomy, Interdisciplinary Nanoscience Center (iNANO), Aarhus University, 8000 Aarhus C, Denmark.

¶Department of Physics, Indian Institute of Technology Bombay, Powai, Mumbai 400076, India.

Notes

The authors declare no competing financial interest.

■ ACKNOWLEDGMENTS

■ REFERENCES

(1) Pla, J. J.; Tan, K. Y.; Dehollain, J. P.; Lim, W. H.; Morton, J. J. L.; Jamieson, D. N.; Dzurak, A. S.; Morello, A. *Nature* **2012**, *489*, 541−545.

(2) Tyryshkin, A. M.; Tojo, S.; Morton, J. J. L.; Riemann, H.; Abrosimov, N. V.; Becker, P.; Pohl, H. J.; Schenkel, T.; Thewalt, M. L. W.; Itoh, K. M.; Lyon, S. A. *Nat. Mater.* **2012**, *11*, 143−147.

(3) Kane, B. E. *Nature* **1998**, *393*, 133−137.

(4) Hollenberg, L. C. L.; Greentree, A. D.; Fowler, A. G.; Wellard, C. J. *Phys. Rev. B* **2006**, *74*, 045311.

(5) Taylor, J. M.; Engel, H.-A.; Dür, W.; Yacoby, A.; Marcus, C. M.; Zoller, P.; Lukin, M. D. *Nat. Phys.* **2005**, *1*, 177−183.

(6) Skinner, A. J.; Davenport, M. E.; Kane, B. E. *Phys. Rev. Lett.* **2003**, *90*, 087901.

(7) Bose, S. *Phys. Rev. Lett.* **2003**, *91*, 207901.

(8) Friesen, M.; Biswas, A.; Hu, X.; Lidar, D. *Phys. Rev. Lett.* **2007**, *98*, 230503.

(9) Greentree, A. D.; Cole, J. H.; Hamilton, A. R.; Hollenberg, L. C. L. *Phys. Rev. B* **2004**, *70*, 235317.

(10) DiVincenzo, D. P.; Bacon, D.; Kempe, J.; Burkard, G.; Whaley, K. B. *Nature* **2000**, *408*, 339−342.

(11) Laird, E. A.; Taylor, J. M.; DiVincenzo, D. P.; Marcus, C. M.; Hanson, M. P.; Gossard, A. C. *Phys. Rev. B* **2010**, *82*, 075403.

(12) Gaudreau, L.; Granger, G.; Kam, A.; Aers, G. C.; Studenikin, S. A.; Zawadzki, P.; Pioro-Ladrière, M.; Wasilewski, Z. R.; Sachrajda, A. S. *Nat. Phys.* **2012**, *8*, 54−58.

(13) Medford, J.; Beil, J.; Taylor, J. M.; Rashba, E. I.; Lu, H.; Gossard, A. C.; Marcus, C. M. *Phys. Rev. Lett.* **2013**, *111*, 050501.

(14) Petta, J. R.; Johnson, A. C.; Taylor, J. M.; Laird, E. A.; Yacoby, A.; Lukin, M. D.; Marcus, C. M.; Hanson, M. P.; Gossard, A. C. *Science* **2005**, *309*, 2180−2184.

(15) Maune, B. M.; Borselli, M. G.; Huang, B.; Ladd, T. D.; Deelman, P. W.; Holabird, K. S.; Kiselev, A. A.; Alvarado-Rodriguez, I.; Ross, R. S.; Schmitz, A. E.; Sokolich, M.; Watson, C. A.; Gyure, M. F.; Hunter, A. T. *Nature* **2012**, *481*, 344−347.

(16) Roche, B.; Dupont-Ferrier, E.; Voisin, B.; Cobian, M.; Jehl, X.; Wacquez, R.; Vinet, M.; Niquet, Y.-M.; Sanquer, M. *Phys. Rev. Lett.* **2012**, *108*, 206812.

(17) Weber, B.; Mahapatra, S.; Watson, T. F.; Simmons, M. Y. *Nano Lett.* **2012**, *12*, 4001−4006.

(18) Gaudreau, L.; Studenikin, S. A.; Sachrajda, A. S.; Zawadzki, P.; Kam, A.; Lapointe, J.; Korkusinski, M.; Hawrylak, P. *Phys. Rev. Lett.* **2006**, *97*, 036807.

(19) Amaha, S.; Izumida, W.; Hatano, T.; Teraoka, S.; Tarucha, S.; Gupta, J. A.; Austing, D. G. *Phys. Rev. Lett.* **2013**, *110*, 016803.

(20) Braakman, F. R.; Barthelemy, P.; Reichl, C.; Wegscheider, W.; Vandersypen, L. M. K. *Nat. Nano* **2013**, *8*, 432−437.

(21) Pan, H.; House, M. G.; Hao, X.; Jiang, H. W. *Appl. Phys. Lett.* **2012**, *100*, 263109.

(22) Amaha, S.; Hatano, T.; Tamura, H.; Teraoka, S.; Kubo, T.; Tokura, Y.; Austing, D. G.; Tarucha, S. *Phys. Rev. B* **2012**, *85*, 081301.

(23) Busl, M.; Granger, G.; Gaudreau, L.; Sánchez, R.; Kam, A.; Pioro-Ladrière, M.; Studenikin, S. A.; Zawadzki, P.; Wasilewski, Z. R.; Sachrajda, A. S.; Platero, G. *Nat. Nano* **2013**, *8*, 261−265.

(24) Fuechsle, M.; Miwa, J. A.; Mahapatra, S.; Ryu, H.; Lee, S.; Warschkow, O.; Hollenberg, L. C. L.; Klimeck, G.; Simmons, M. Y. *Nat. Nano* **2012**, *7*, 242−246.

(25) Fuhrer, A.; Fuechsle, M.; Reusch, T. C. G.; Weber, B.; Simmons, M. Y. *Nano Lett.* **2009**, *9*, 707−710.

(26) Fuechsle, M.; Mahapatra, S.; Zwanenburg, F. A.; Friesen, M.; Eriksson, M. A.; Simmons, M. Y. *Nat. Nano* **2010**, *5*, 502−505.

(27) Mahapatra, S.; Büch, H.; Simmons, M. Y. *Nano Lett.* **2011**, *11*, 4376−4381.

(28) Büch, H.; Mahapatra, S.; Rahman, R.; Morello, A.; Simmons, M. Y. *Nat. Commun.* **2013**, *4*, 2017.

(29) McKibbin, S. R.; Clarke, W. R.; Fuhrer, A.; Reusch, T. C. G.; Simmons, M. Y. *Appl. Phys. Lett.* **2009**, *95*, 233111.

(30) Weber, B.; Mahapatra, S.; Ryu, H.; Lee, S.; Fuhrer, A.; Reusch, T. C. G.; Thompson, D. L.; Lee, W. C. T.; Klimeck, G.; Hollenberg, L. C. L.; Simmons, M. Y. *Science* **2012**, *335*, 64−67.

(31) Nabors, K.; White, J. *IEEE Trans. Comput.-Aided Des. Integr. Circuits Syst.* **1991**, *10*, 1447−1459.

(32) Schröer, D.; Greentree, A. D.; Gaudreau, L.; Eberl, K.; Hollenberg, L. C. L.; Kotthaus, J. P.; Ludwig, S. *Phys. Rev. B* **2007**, *76*, 075306.

(33) Granger, G.; Gaudreau, L.; Kam, A.; Pioro-Ladrière, M.; Studenikin, S. A.; Wasilewski, Z. R.; Zawadzki, P.; Sachrajda, A. S. *Phys. Rev. B* **2010**, *82*, 075304.

(34) Rogge, M. C.; Haug, R. J. *New J. Phys.* **2009**, *11*, 113037.